scientific reports

OPEN

Characterizing variability in passive myocardial stiffness in healthy human left ventricles using personalized MRI and finite element modeling

Fikunwa O. Kolawole[1,2,3,4]✉, Vicky Y. Wang[1,2,5], Bianca Freytag[6], Michael Loecher[1,2], Tyler E. Cork[1,2,4,7], Martyn P. Nash[5], Ellen Kuhl[3] & Daniel B. Ennis[1,2,4]

Abnormal passive stiffness of the heart muscle (myocardium) is evident in the pathophysiology of several cardiovascular diseases, making it an important indicator of heart health. Recent advancements in cardiac imaging and biophysical modeling now enable more effective evaluation of this biomarker. Estimating passive myocardial stiffness can be accomplished through an MRI-based approach that requires comprehensive subject-specific input data. This includes the gross cardiac geometry (e.g. from conventional cine imaging), regional diastolic kinematics (e.g. from tagged MRI), microstructural configuration (e.g. from diffusion tensor imaging), and ventricular diastolic pressure, whether invasively measured or non-invasively estimated. Despite the progress in cardiac biomechanics simulations, developing a framework to integrate multiphase and multimodal cardiac MRI data for estimating passive myocardial stiffness has remained a challenge. Moreover, the sensitivity of estimated passive myocardial stiffness to input data has not been fully explored. This study aims to: (1) develop a framework for integrating subject-specific *in vivo* MRI data into *in silico* left ventricular finite element models to estimate passive myocardial stiffness, (2) apply the framework to estimate the passive myocardial stiffness of multiple healthy subjects under assumed filling pressure, and (3) assess the sensitivity of these estimates to loading conditions and myofiber orientations. This work contributes toward the establishment of a range of reference values for material parameters of passive myocardium in healthy human subjects. Notably, in this study, beat-to-beat variation in left ventricular end-diastolic pressure was found to have a greater influence on passive myocardial material parameter estimation than variation in fiber orientation.

Keywords Cardiac mechanics, *In vivo* cardiac MRI, Inverse FEM, Passive myocardial stiffness

Altered passive stiffness of myocardium, the heart's muscular tissue, is a key feature of maladaptive cardiac remodeling and is implicated in the etiology of several heart diseases including heart failure[1]. As an important biomarker of overall heart function, accurately identifying changes in passive myocardial stiffness can improve heart disease diagnosis and management. Although passive myocardial stiffness can clinically be inferred from the end-diastolic pressure-volume relationship of the left ventricle (LV), this measure reflects an apparent stiffness affected by ventricular geometry, rather than intrinsic myocardial stiffness. For example, a thicker heart wall requires more force to deform compared to a thinner heart wall of the same intrinsic stiffness. This results in higher apparent stiffness, though the intrinsic material stiffness remains constant.

The mechanisms driving changes in passive myocardial stiffness and their effects on heart disease progression are not yet fully understood. This gap has led to the development of cardiac biophysical models

[1]Department of Radiology, Stanford University, Stanford, CA 94305, USA. [2]Division of Radiology, Veterans Administration Health Care System, Palo Alto, CA 94304, USA. [3]Department of Mechanical Engineering, Stanford University, Stanford, CA 94305, USA. [4]Cardiovascular Institute, Stanford University, Stanford, CA, USA. [5]Auckland Bioengineering Institute, University of Auckland, Auckland, New Zealand. [6]University of Grenoble Alpes, CNRS, TIMC UMR 5525, 38000 Grenoble, France. [7]Department of Bioengineering, Stanford University, Stanford, CA 94305, USA. ✉email: fikunwa@stanford.edu

aimed at estimating the material parameters governing the mechanical behavior and stiffness of *in vivo* passive myocardium. The mechanical behavior of a material can be described by a constitutive relation which defines the relationship between stress and strain under various loading conditions, through a set of material parameters.

MRI-based inverse finite element modeling (FEM) has proven effective for identifying subject-specific passive myocardial stiffness, as demonstrated by several research groups[2–4]. Recent contributions to the field of MRI-based cardiac mechanics include validation[5], uncertainty quantification[6,7], assessing the impact of boundary conditions[8,9] and residual strains[10], improvement of the optimization strategy[11], development of constitutive models of myocardium[12], and improving the identifiability of passive myocardial stiffness[13].

When provided with cardiac geometry, microstructural configuration of cardiomyocytes, boundary conditions, kinematics, and end-diastolic (filling) pressure(s), then inverse FEM methods can be used to derive the parameters of the material law that describe the myocardium's mechanical behavior. End-diastolic pressure(s) can be measured invasively through catheterization or estimated non-invasively (e.g. by mitral flow velocity[14]). Cardiac surface geometry is best determined from conventional cine balanced steady-state free-precession (bSSFP) MRI as it offers exceptional signal-to-noise ratio and high contrast between myocardium and blood, facilitating excellent delineation of endocardial and epicardial borders[15]. Local kinematics, a measure of the deformation of specific regions of the heart, can be measured using tagged MRI[16] or cine DENSE MRI[17], and cardiac microstructure can be assessed non-invasively using *in vivo* cardiac diffusion tensor imaging (cDTI)[18]. However, to our knowledge, no study has integrated subject-specific *in vivo* cDTI, cine bSSFP, and tagged MRI into personalized *in silico* passive mechanics models. This is partly due to the challenge of acquiring comprehensive, high-fidelity imaging data and the lack of an established framework for combining these benchmark data into a single personalized *in silico* mechanics model. Additionally, there is a need to better characterize the range of healthy *in vivo* myocardial behavior to improve our understanding of cardiac dysfunction.

Herein, we acquired high fidelity *in vivo* MRI data-including cine bSSFP, tagged MRI, and cDTI-from healthy adult subjects (N=7) with no cardiovascular disease (male & female, 22-32 years, BMI 22-28). We developed a framework for integrating all the subject-specific MRI data into FEM representations of the left ventricle (LV). Using this framework, we calibrated the passive myocardial stiffness of each subject's personalized LV mechanics model based on local kinematics. In addition, we evaluated how variations in cardiomyocyte orientations and loading conditions affect the estimated passive myocardial material parameters. This study not only provides a range of reference values for passive myocardial stiffness in healthy individuals, but also demonstrates the influence of different factors on variability in these estimates.

Methods

Image acquisition

This study was conducted in accordance with the ethical principles outlined in the Declaration of Helsinki. All participants signed statements of informed consent, and the research protocol was approved by the Institutional Review Board at Stanford University. Each subject (Table 2) underwent a comprehensive 90-minute *in vivo* MRI exam using a 3T scanner (Skyra, Siemens), during which cine bSSFP, cDTI, and tagged MRI datasets were acquired (Fig. 1). These images fully covered the LV from base to apex.

In vivo cine bSSFP images were acquired in both short and long axis with retrospective gating (TE/T_{Res} = 1.49/35.0 ms; FA = 35°; resolution = $1\times1\times6$ mm^3; 4 mm slice gap; 25 cardiac phases). Short and long-axis tagged images were acquired with the same spatial and temporal resolution as the cine bSSFP, also using a

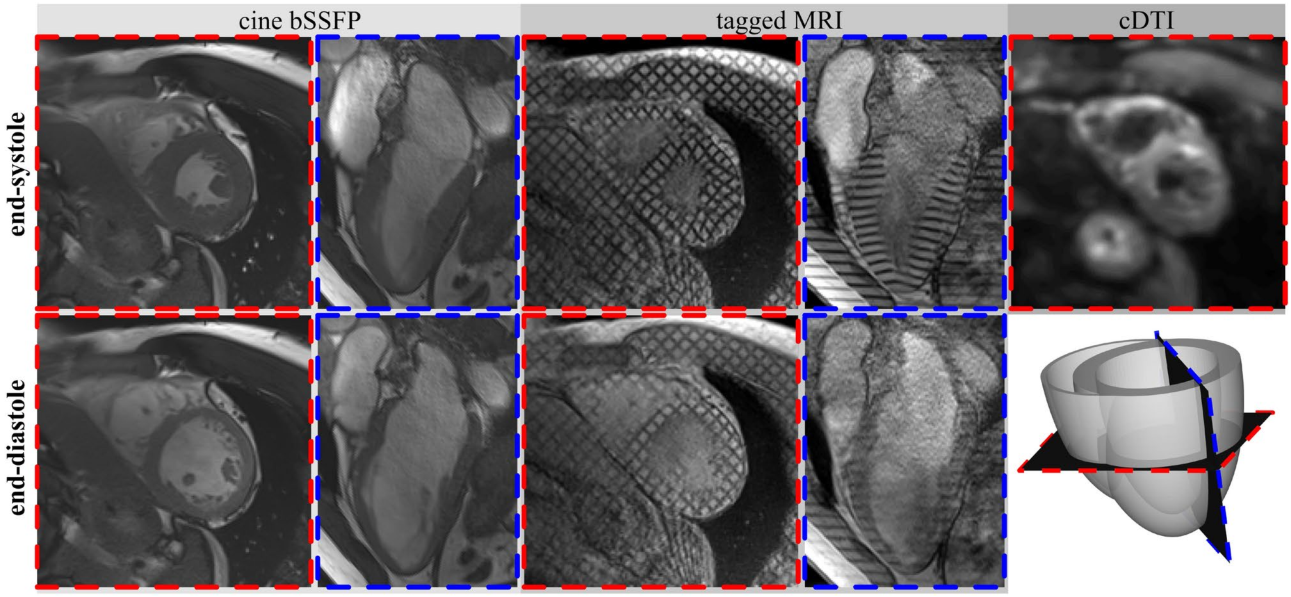

Fig. 1. Representative cine bSSFP, tagged MRI, and cDTI (b=0) images from one subject showing both short and long-axis views at end-systole and end-diastole.

retrospectively gated sequence. In the short axis, grid tagged images were obtained (TE/T_{Res} = 3.01/31.50 ms; FA = 12°; resolution = 1×1×6 mm^3; 4 mm slice gap; 25 cardiac phases; 7 mm tag spacing) and in the long-axis, images with radially oriented line tags were acquired (TE/T_{Res} = 2.8/46.08 ms; FA = 10°; resolution = 1×1×10 mm^3, 10 mm slice thickness, 3 slices). The first long-axis image bisected a central region of the interventricular septum and the LV free wall, another intersected the posterior RV insertion point and the anterior papillary muscle, and the third crossed the anterior RV insertion point and posterior papillary muscle.

Following the tagged MRI acquisition, *in vivo* cDTI were acquired using a navigator-based free-breathing, slice-following, spin-echo Echo Planar Imaging (EPI) sequence with symmetric first and second-order motion-compensated diffusion gradients[19] (TE/TR = 86/3×R-R interval; resolution = 2×2×8 mm^3; 2 mm slice gap; b-values = [0, 350] s/mm^2; number of diffusion directions = 15; Averages = 5; Partial Fourier = 6/8; GRAPPA = 2). Using a trigger delay (200 - 300ms), two separate cDTI datasets were acquired at end-systole with reversed phase encoding directions (referred to as blip-up and blip-down) to mitigate image distortion artifacts.

Geometric analysis from cine bSSFP

The first pre-processing step necessary for some of the cine bSSFP data was slice alignment. In cine MRI, each slice is acquired in a single breath-hold during which images of the entire cardiac cycle are obtained. Slice misalignment can arise due to breath hold differences and subject motion. To address this, we developed a contour-based slice alignment method that minimizes the distance between the long-axis and short-axis endocardial contours. First, the long-axis slices were aligned by ensuring the endocardial contours intersected. Next, each short-axis slice was aligned by applying a best-fit (least squares) translation to match its endocardial contour with those of the long-axis. This process was repeated for each short-axis slice until all the long-axis and short-axis images were co-registered (Fig. 2).

The cine bSSFP images were then processed using Cardiac Image Modeller (CIM, version 8.2, University of Auckland, New Zealand), which facilitated semi-automated segmentation of the LV surfaces over the entire imaging cycle (Fig. 3). Specifically, landmark points at the LV basal centroid, right ventricular basal centroid, and LV apex were manually identified and subsequently used to construct an initial LV surface representation in an orthogonal cardiac coordinate system. In this coordinate system, the origin was positioned one-third of the distance along the longitudinal axis from the LV base to the apex. The x, y, and z axes were aligned towards the LV apex, the right ventricular centroid, and the posterior LV wall, respectively. LV endocardial and epicardial surfaces were interactively generated for all cardiac phases in CIM by fitting the initial LV surface geometry to guide-points placed by the analyst. The reference (load-free) FEM geometry was chosen as the diastasis phase which corresponds to the start of atrial systole[20,21], and the timing was confirmed through the mitral valve

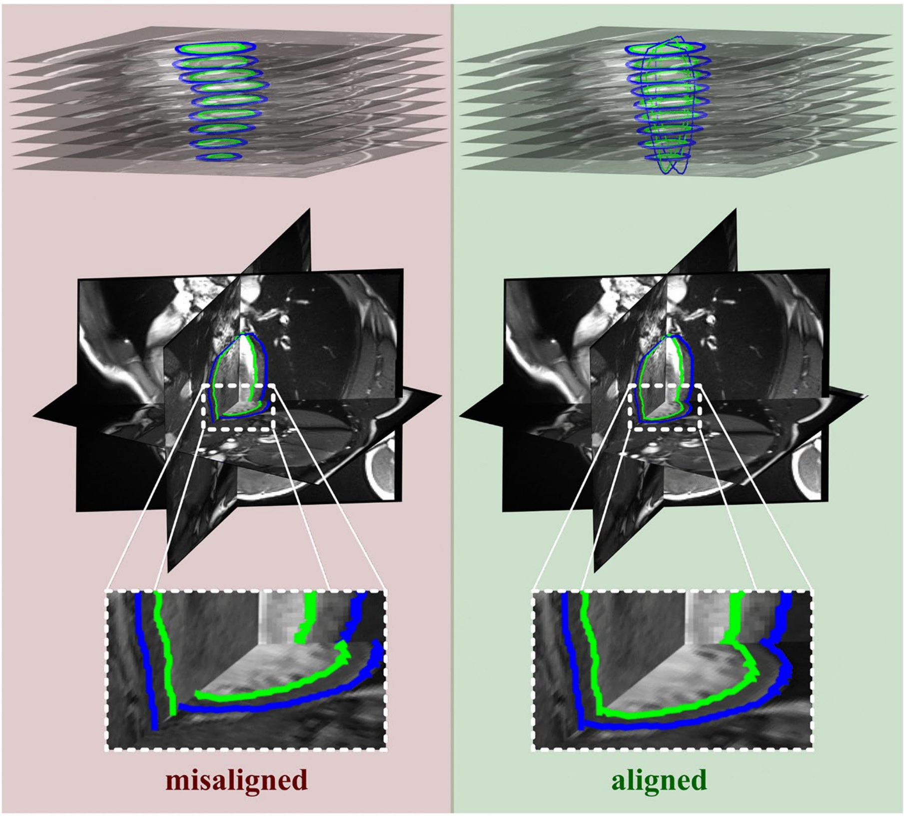

Fig. 2. Cine bSSFP image slice alignment. Slice misalignment due to breath-hold differences and subject motion was corrected using a contour-based approach.

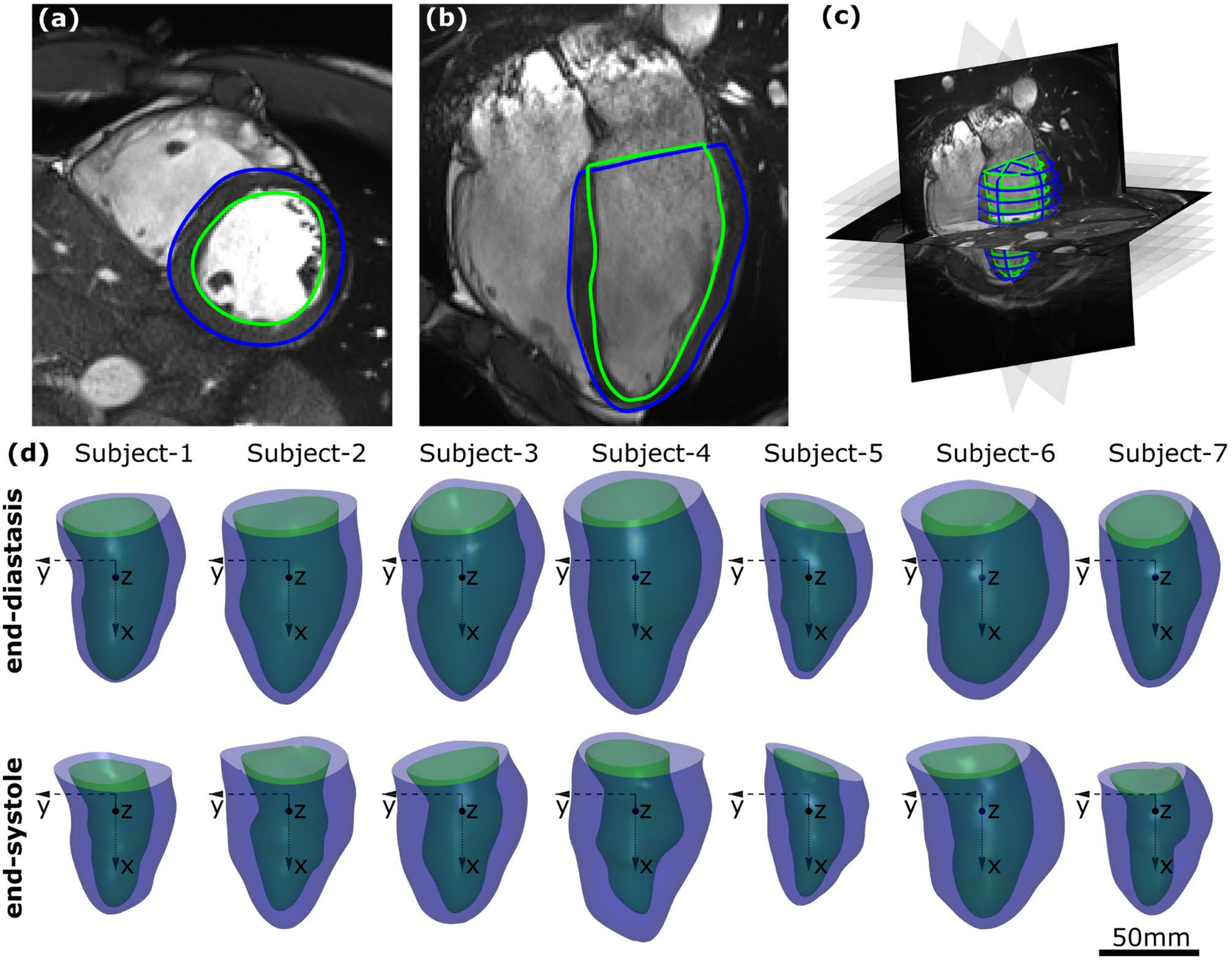

Fig. 3. LV surface geometry generation from cine bSSFP images. A surface model was fit to guide points placed on the (**a**) short and (**b**) long-axis images. (**c**) Intersection of the LV surface geometry with all the images. (**d**) Final diastasis and end-systolic surface geometries for all subjects. All are scaled uniformly by the same amount and a scale bar is included. The endocardial surface is colored green and the epicardial surface is colored blue.

motion observed in the cine bSSFP long-axis images. Cardiac metrics such as the LV end-diastolic volume, end-systolic volume, stroke volume, and wall thickness were extracted from the LV surface geometric models (Table 2).

Kinematics analysis from tagged MRI

First, tagged MRI and cine bSSFP data were registered. The short-axis grid-tagged image slices were registered to the cine bSSFP images by aligning the epicardial contours. This 2D registration was possible because the tagged and cine bSSFP image datasets were spatially and temporally aligned. For long-axis tagged data, registration was achieved by aligning the epicardial outline with the bSSFP-derived epicardial diastasis surface. The registration of the long and short-axis tagged MRI data was limited to in-plane translations. Since the reference geometry for the FEM was constructed at diastasis, the registration was performed on the diastasis images and the resultant transformation was applied to images acquired at all other cardiac phases.

Following registration of the tagged MRI to the cine bSSFP images, a set of myocardial points were defined in the diastasis phase of the grid-tagged images by masking out the LV myocardium using the diastasis LV endocardial and epicardial surfaces. Subsequently, we used a validated machine learning algorithm[22] to track the local myocardial displacements across the cardiac cycle relative to the diastasis phase.

Personalized microstructure analysis from cDTI

For each subject, the blip-up and blip-down cDTI datasets were processed through a customized image post-processing pipeline (CarDpy) that included Gibbs ringing correction[23], shot-rejection, respiratory sorting, and 2D rigid registration, to optimize the signal intensity and spatial localization, mitigating effects of respiratory motion. Next, the five averages of the blip-up and blip-down datasets were retrospectively combined into a complete dataset, which was distortion corrected using the TOPUP algorithm from the FSL package (Fig. 4)[24,25]. Since the cDTI data was acquired at end-systole, the distortion corrected cDTI images were registered to the end-systolic bSSFP images by aligning the epicardial contours. The bSSFP-derived end-systolic LV surface was then used to intersect the cDTI images to identify regions within the LV myocardium. Finally, diffusion tensors for each image voxel within the LV myocardium were reconstructed using non-linear least squares regression[26].

It is important to note that spin-echo motion-compensated techniques, used for the cDTI acquisition, are only reliable during systole[18,27]. Therefore, we acquired the cDTI images at end-systole, though the FEM reference geometry was constructed at diastasis. Consequently, we needed to integrate microstructural information (cardiomyocyte orientation) from the *in vivo* cDTI diffusion tensors acquired at end-systole into the FEM geometric model of the left ventricle, which was obtained at diastasis. To achieve this, we implemented a two-step approach.

The first step involved reconfiguring the raw diffusion tensor data from end-systole to diastasis using the kinematic field derived from tagged MRI analysis. To map the positions of the diffusion tensors from end-systole to diastasis, we first deformed the diastasis LV geometric surface model to end-systole using the kinematic field. The end-systolic diffusion tensor locations were then aligned with this kinematically deformed LV geometry and translated to their diastasis positions using the same kinematic field. To adjust the orientation of the diffusion tensors, we interpolated a deformation gradient tensor between the end-systole and diastasis phases for each voxel within the myocardium. The rotational component of this tensor, derived through polar decomposition, was used to reorient the diffusion tensors to the diastasis state. This method of reorienting myofiber direction data based on the kinematic field was validated *in silico*. Similar kinematics-based diffusion tensor reconfiguration approaches have been implemented previously[28,29].

The second step focused on interpreting these reconfigured diffusion tensors of myocardium slices within the diastasis 3D LV geometric model, using a field-based fitting approach developed and validated by Freytag *et al*[30]. A microstructural orientation field defined by the fiber, imbrication, and sheetlet (Euler) angles, was initialized at each node of a the LV diastasis FE model (total of 34 nodes) and interpolated over the FE model using tricubic Hermite basis functions. The fiber angles, defined as the elevation angle between a fiber vector projected to the LV surface and the local circumferential direction, were initially set to be $+60^\circ$ for the endocardial nodes, and -70° for the epicardial nodes. The imbrication angles, defined as the angle between the fiber vector and its projection to the LV surface, were set to 0°. A local representation of this microstructural orientation field, expressed as the fiber vector $\mathrm{f}_{(v)}$, at each voxel v was computed. The nodal angular parameters describing the fiber vector field were optimized to maximize the alignment of $\mathrm{f}_{(v)}$ with the direction of maximal diffusion. The

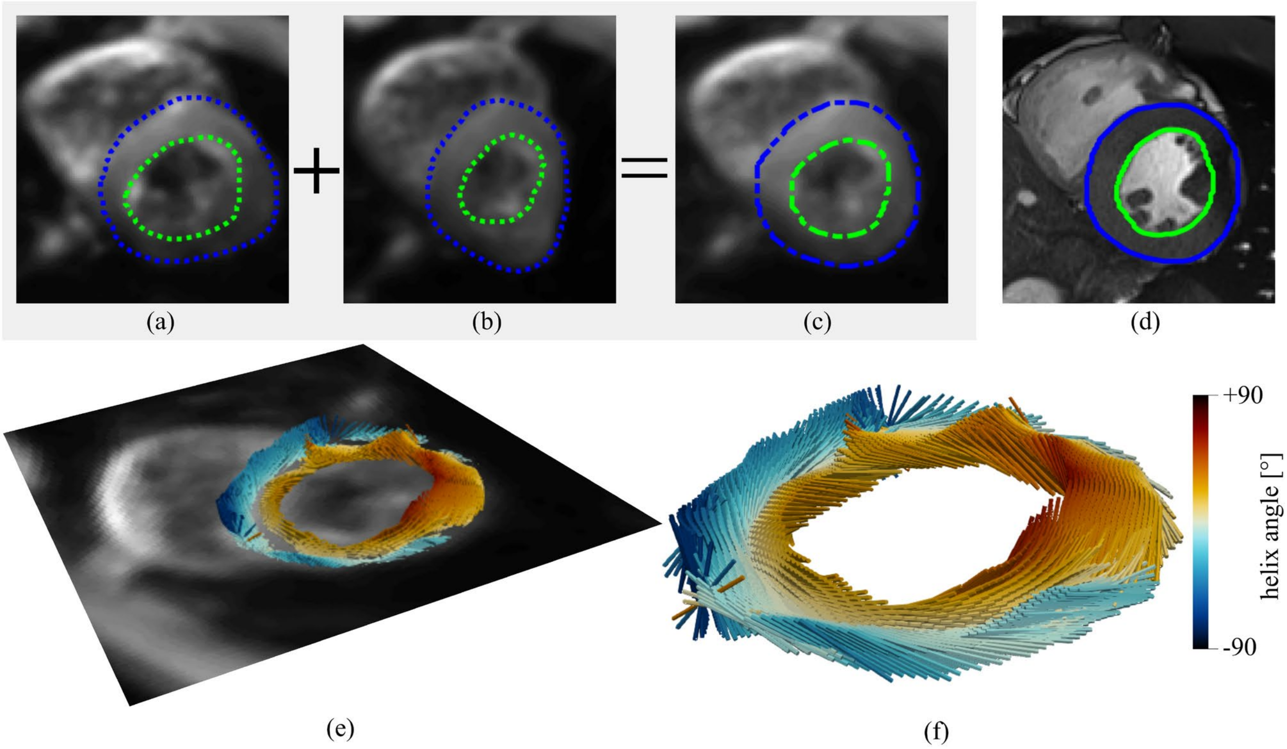

Fig. 4. cDTI geometric distortion is corrected by combining the (**a**) blip-up and (**b**) blip-down images using TOPUP and the FSL package. (**c**) The geometrically corrected images correspond better to the (**d**) cine bSSFP images. Manually contoured epicardial (blue) and endocardial (green) outlines are overlayed on the images. (**e**) the myocardial diffusion tensors are calculated on each slice of the geometrically corrected images. (**f**) The primary eigenvectors of the diffusion tensors for a representative slice colored by the fiber angle (helix angle) are shown.

objective function was expressed as the dot product of $f_{(v)}$ with the projection of the diffusion tensor ($D_{(v)}$) in the direction of $f_{(v)}$. Only fiber and imbrication angles were fitted. Optimization of the fiber orientation field was performed using the software package CMGUI[31] following procedures outlined by Freytag *et al.*[30]. The 3D description of the fiber orientation at diastasis was subsequently incorporated into the *in silico* LV model.

Rule-based microstructure description

Subject-specific microstructural imaging with *in vivo* cDTI is only recently available in patients or research subjects[17,32,33]. Moreover, processing and integrating cDTI-obtained microstructural information into FE mechanics models can be prohibitively cumbersome. This has motivated the development of several mathematical descriptions of myofiber orientation[34–36] which are used in the absence of personalized *in vivo* estimates of cardiac microstructure.

One such widely used approach is the Laplace-Dirichlet rule-based (LDRB) algorithm, introduced by Bayer *et al.*[34]. To create a continuous fiber orientation description throughout the LV myocardium, the LDRB algorithm requires definition of the basal, epicardial, and endocardial surfaces, along with the specification of helical and transverse angles on the epicardial and endocardial boundaries. The helical angle (θ) is the degree to which cardiomyoctes are angled out of the short-axis plane, while the transverse angle (β) is between the longitudinal axis of the cardiomyocyte and the local circumferential direction. θ and β are defined at a transmural depth *d* normalized from 0 to 1 as:

$$\theta(d) = \theta_{endo}(1-d) + \theta_{epi} * d \tag{1a}$$

$$\beta(d) = \beta_{endo}(1-d) + \beta_{epi} * d. \tag{1b}$$

In our study, we explored nine different rule-based fiber descriptions for each subject. These descriptions varied across a range of θ_{endo} from 30° to 90° and θ_{epi} from -30° to -90°. These nine cases, shown in fig. 5, are referred to as $R_{i,j}$ with *i* and *j* referring to θ_{endo} and θ_{epi} respectively. For example, $R_{60,-90}$ represents a rule-based description with $\theta_{endo} = 60^\circ$ and $\theta_{epi} = -90^\circ$. Across all models, β was set to 0° on the epicardial and endocardial surfaces, since there is evidence that the transverse angle stays relatively constant and close to zero throughout the myocardial wall[37].

Constitutive relation

The myocardium was modeled as a hyperelastic incompressible material using a transversely isotropic exponential constitutive relation[38] described by the following strain energy density function:

$$\begin{aligned} \psi &= \frac{1}{2}c(e^Q - 1) \\ Q &= b_f E_{ff}^2 + b_t(E_{ss}^2 + E_{nn}^2 + 2E_{sn}^2) + 2b_{ft}(E_{fs}^2 + E_{fn}^2) \end{aligned} \tag{2}$$

where the *c* parameter scales the overall passive myocardial stiffness and the b_f, b_t, and b_{ft} parameters assign different exponential responses in the fiber (*f*) direction, across transverse (*t*) planes orthogonal to the fiber, and along the shear plane between the fiber and transverse direction (*ft*). E_{ij} denotes the components of the Green-Lagrange strain tensor (***E***) in a local myocardial coordinate system consisting of the fiber (*f*), sheetlet (*s*) and sheetlet normal (*n*) directions.

We used the reformulation proposed by Xi *et al.*[39] that expresses the strain energy law in terms of *c*, α, r_f, and r_t, described in terms of the original formulation's parameters as:

$$\alpha = b_f + b_t + b_{ft}; \quad r_f = \frac{b_f}{\alpha}; \quad r_t = \frac{b_t}{\alpha}; \quad r_{ft} = \frac{b_{ft}}{\alpha} = 1 - r_f - r_t \tag{3}$$

$$Q = \alpha r_f E_{ff}^2 + \alpha r_t(E_{ss}^2 + E_{nn}^2 + 2E_{sn}^2) + 2\alpha(1 - r_f - r_t)(E_{fs}^2 + E_{fn}^2) \tag{4}$$

Following this reformulation, the material behavior is readily interpreted as the homogenous stiffness scaling parameters (*c* and α), and the anisotropy ratios in the fiber and transverse directions (r_f and r_t). The reformulation also encapsulates the non-uniqueness and correlation of parameters of the transversely isotropic law in the space of *c* and α.

Passive material parameter estimation

The FE mechanics analysis was limited to the passive filling phase from diastasis to end-diastole. The LV diastasis geometric model was used as the reference mechanics model, (section Geometric analysis from cine bSSFP) and was meshed with standard quadratic tetrahedral elements using GMSH[40]. The final mesh characteristics were determined following a mesh sensitivity study and are detailed in table 1. The FE model was then built to be solved in FEBio[41].

Clinically, a normal LV end-diastolic pressure is typically characterized as ranging from 4-12 mmHg with an average of approximately 8 mmHg[42]. Therefore, in the absence of measured subject-specific LV cavity pressure recordings, the *in silico* LV was passively inflated by applying an endocardial pressure of 8 mmHg. Motivated by

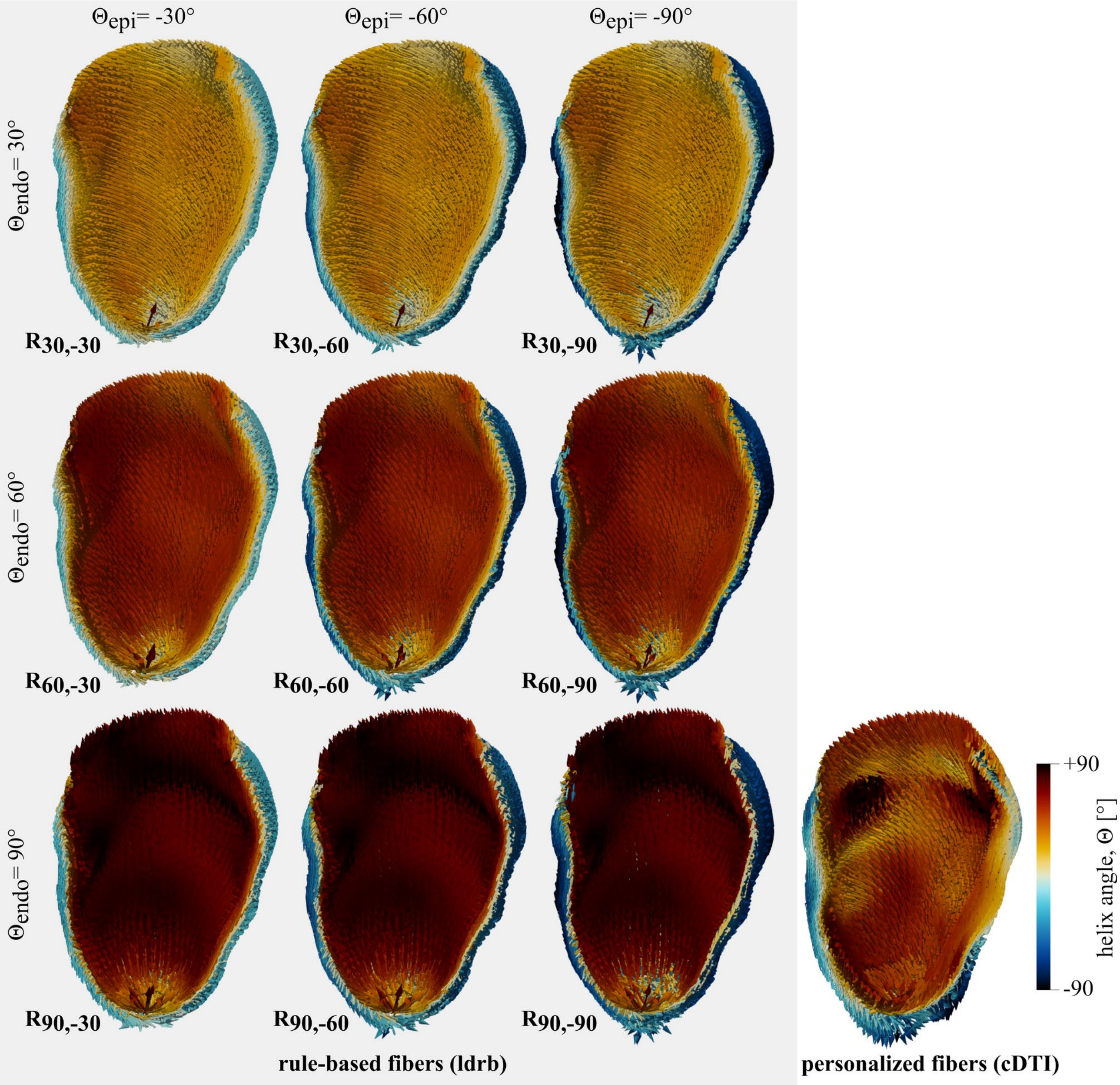

Fig. 5. Different fiber orientations tested for each subject. Myofiber orientations were personalized using *in vivo* cDTI and alternatively described using the rule-based LDRB algorithm[34]. θ is the helix angle.

Case	Nodes	Elements	Element Volume (mm^3)
Subject-1	37,268	22,420	3.54
Subject-2	55,631	35,370	3.40
Subject-3	55,494	35,018	3.43
Subject-4	76,484	49,039	3.48
Subject-5	32,226	19,549	3.42
Subject-6	74,933	48,305	3.33
Subject-7	37,868	23,069	3.42

Table 1. Mesh Properties.

a study by Hasaballa *et al.* which quantified the beat-to-beat variation in LV end-diastolic chamber stiffness in controls[43], the uncertainty in the simulated material parameters due to a ±20% uncertainty in LV end-diastolic pressure was also investigated. Dirichlet boundary conditions were applied to constrain the longitudinal displacements of the *in silico* model's basal nodes to match the tagged MRI-derived kinematics. In the short-axis, only LV basal nodes belonging to the epicardial ring were fixed, while the remaining nodes were unconstrained. Then, the experimentally determined LV local displacements from diastasis to end-diastole were used to inversely estimate the optimal parameters of the reformulated transversely isotropic exponential constitutive relation (section 2.6). Note that our *in silico* mechanics model is two-state, only considering the reference state at diastasis and the maximum inflation state at end-diastole. This was done to avoid assuming the form of the diastolic pressure waveform given the notable variability among subjects[44].

Fung-type exponential constitutive relations are known to provide stress-strain relations that are non-unique with respect to the constitutive parameters. In the case of the the reformulated transversely isotropic relation used here, there exists a set of nearly kinematically equivalent stress-strain relations in the space of *c* and α. Here, we present the results of the passive mechanical behavior as optimal *c*-α coupling curves that encapsulate the set of non-unique solutions. The anisotropy ratios, which reflect the variation in stiffness along the fiber, transverse and shear planes, were kept constant at physiologically realistic values of $r_f = 0.55$, $r_t = 0.25$, and $r_{ft} = 0.2$ given that the stiffest behavior is expected to be along the fiber direction[13]. As demonstrated by Xi *et al.* the *c*-α coupling curve can be described by the relationship $\alpha c^a = b$. Given the linear nature of the coupling curve in log-space, with the form of $a \log c + \log \alpha = \log b$, to find the optimal *c*-α coupling curve that characterizes the non-unique passive material properties, at least two parameter optimizations are required at different α values.

To determine the optimal *c*-α coupling curve for each subject, simulations were performed to find the values of *c* corresponding to the minimal-residual solutions for three logarithmically spaced values of α (10, 32, and 100). Specifically, for each alpha value, after initializing the *c* material parameter using results from Nasopoulou *et al.*[13], we iteratively updated *c* to minimize the displacement error ($|\Delta u_{sim-exp}|$). Given experimentally measured end-diastolic nodal positions from tagged MRI (x_{exp}), and simulated pressure-induced end-diastolic nodal positions (x_{sim}), the displacement error is calculated as $|\Delta u_{sim-exp}| = |x_{exp} - x_{sim}|$. Subsequently, after identifying three pairs of optimal *c* and α, a straight line was fit to the three pairs of optimal *c* and α points in log-space to identify the optimal relationship between *c* and α for the given geometric and kinematic data.

The procedure for developing the forward FE mechanics models and the material parameter identification methodology is summarized in fig. 6.

Results

Subject demographics and heart metrics are shown in table 2. Subjects were all within a healthy range for heart metrics[45]. Across all subjects, the identified optimal *c* and α value pairs provided a good match between the end-diastolic nodal positions predicted by the FE simulation and those measured from the tagged MRI. Figure 7 shows the displacement error between the experimental and simulated nodal positions for all subjects. An optimal *c*-α coupling curve which provided a good fit to the pairs of optimal *c* and α points ($R^2 > 0.99$) was identified for each subject (Fig. 8).

Figure 8 overlays each subject's optimal *c*-α coupling curve for the FE model with personalized fibers with uncertainty due to a ±20% end-diastolic pressure variability[43]. The figure also shows the same result for the range of rule-based fiber descriptions tested. As a comparison, healthy *in vivo* passive myocardial material parameters from literature are also overlayed with our results.

Figure 9 shows the mechanical behavior in uniaxial tension using the optimal material parameters at $\alpha = 32$ for each subject. Note that the poor cDTI acquisition in Subject-4 prevented the development of a personalized fiber FE model for this subject. Hence, for this subject, we show results for the $R_{60,-60}$ fiber description.

We more directly compare the observed variation in the estimated material parameters due to the loading pressure and rule-based fiber variability in fig. 10. In all subjects, the parameter variation due to the end-diastolic pressure uncertainty exceeded the variation due to rule-based fiber orientation variability.

Using the estimated parameters (at $\alpha = 32$), we calculated the fiber Cauchy stress and stretch. The distribution of fiber stress and stretch for each subject is shown in fig. 11. There wasn't a substantial variation in the fiber stress and stretch distribution for different values of c and α that fall along the optimal coupling curve (<0.6% difference on average).

Table 3 shows the estimated *c* parameter at $\alpha = 32$ for all subjects. The average fiber Cauchy stress, fiber stretch and displacement error between the FE-predicted nodal positions and the tagged MRI-derived target nodal positions are also listed. For all the metrics in Table 3, we also show the minimum and maximum range from alternate simulations using the different rule-based descriptions of microstructure evaluated in this study (Fig. 5).

To put the subjects' estimated parameters in context, results from three previously published studies that performed passive myocardial parameter estimation in healthy humans are compared. In fig. 8h, we overlay the parameters obtained in Nasopoulou *et al.*[13], Wang *et al.*[46], and Xi *et al.*[39] over the optimal *c*-α coupling curves for all the subjects. We also do this comparison with the literature in terms of principal Cauchy stress and stretch in a simulated idealized unixial tensile test using the material parameters. Specifically, using the optimal *c*-α coupling curve for a subject, we found the *c* parameter that corresponds to a given α from the literature study. The obtained optimal *c* and α combination for the subject was then used to simulate the mechanical behavior (Cauchy stress vs. stretch) in uniaxial tension along the fiber direction. This mechanical behavior across all subjects is compared with the literature results in fig. 12.

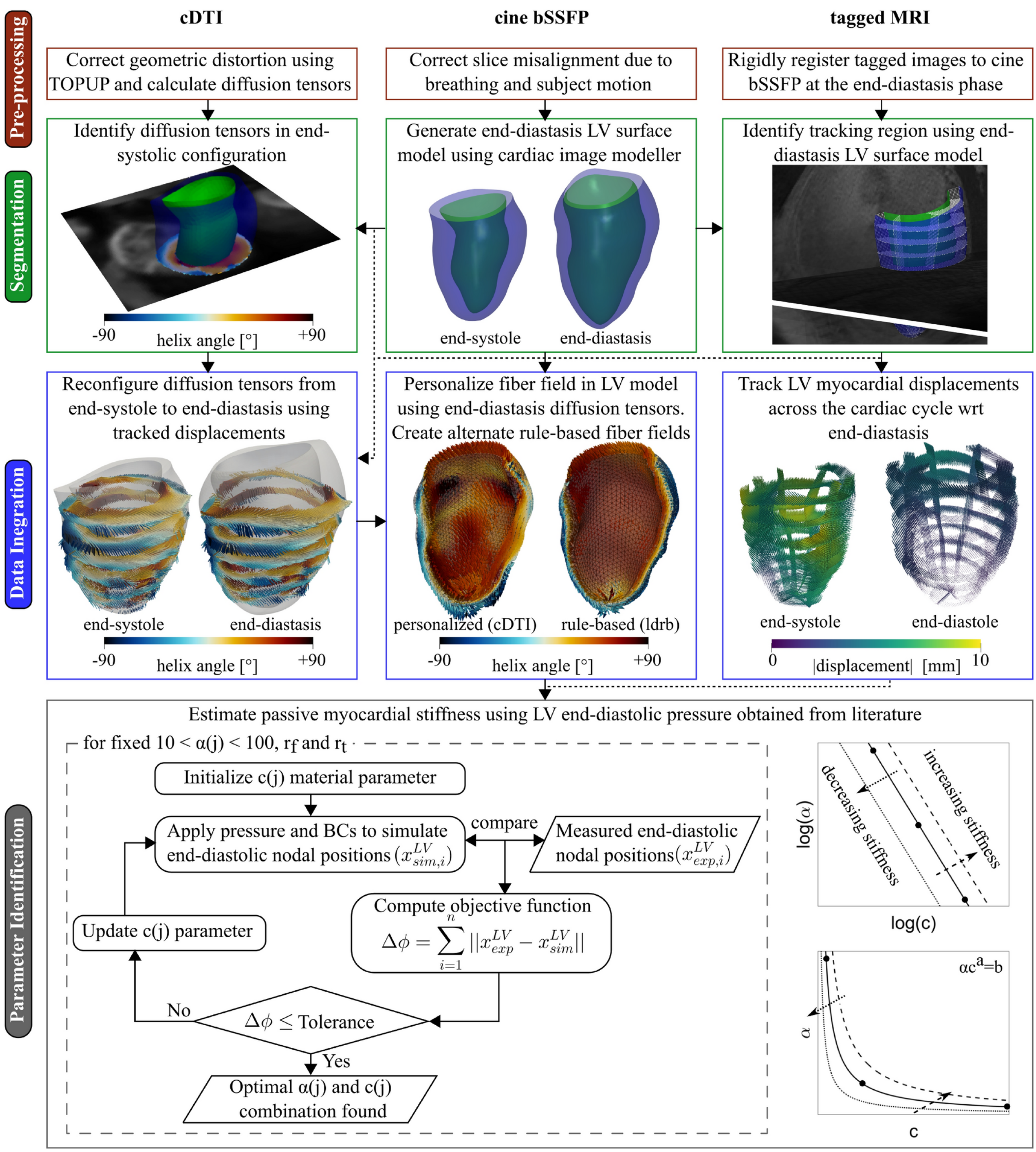

Fig. 6. Pipeline for integrating geometry (cine bSSFP), microstructure (cDTI), and kinematics (tagged MRI) data into a finite element mechanics model for estimating passive myocardial stiffness. The material parameter estimation procedure using the forward FE mechanics model and the kinematic data is also summarized.

Discussion

Computational cardiac biomechanics enables integration of detailed geometric, functional, and microstructural data extracted from cardiac imaging tools to predict key aspects of heart function such as passive myocardial stiffness, which influences the heart's filling. The capability of estimating intrinsic passive myocardial stiffness has clinical applications including disease diagnosis, stratification, treatment planning, and therapy monitoring[3,4,47]. While previous studies have used medical imaging and inverse FE modeling to evaluate passive myocardial stiffness, to our knowledge, we are the first to combine *in vivo* cine MRI, tagged MRI, and cDTI to create subject-specific FE models.

Case	Sex	Age (yrs)	BMI (kg/m^2)	LV mass (g)	EDV (ml)	ESV (ml)	EF (%)	WT (mm)
Subject-1	F	25	22.7	83.8	131.5	46.5	64.6	5.7±0.6
Subject-2	M	29	27.8	128.1	151.2	65.9	56.4	7.7±0.8
Subject-3	M	32	23.1	131.6	165.3	67.9	59.0	7.5±0.9
Subject-4	M	24	26.9	182.3	226.1	80.8	64.3	8.3±0.6
Subject-5	F	22	21.9	69.7	89.9	39.8	55.7	6.2±0.4
Subject-6	M	25	27.5	170.9	196.7	92.7	52.9	8.5±1.0
Subject-7	F	26	24.9	81.3	118.4	42.0	64.6	6.5±0.8

Table 2. Subject demographics and heart metrics. F/M = female/male, BMI = body mass index, EDV = LV end-diastolic volume, ESV = LV end-systolic volume, EF = LV ejection fraction, WT = LV wall thickness in diastasis presented as mean±std of values from the inferoseptal, inferior, inferolateral, anterolateral, anterior, and anteroseptal LV regions.

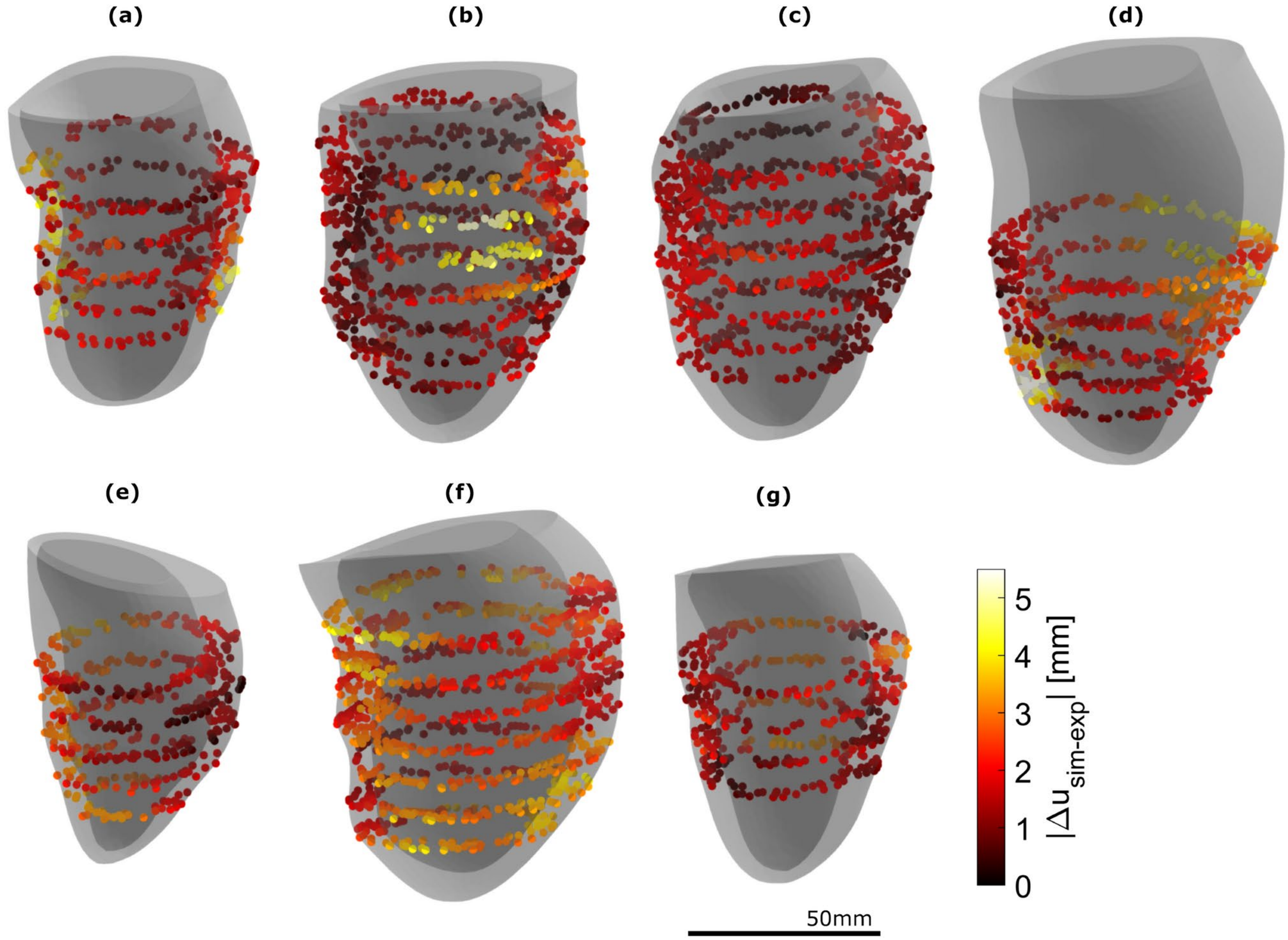

Fig. 7. Displacement error ($|\Delta u_{sim-exp}|$) between experimentally determined nodal positions and simulated nodal positions using one optimal c and α combination. In all subjects, the experimentally measured and simulated end-diastolic nodal positions matched well. All surface geometries are scaled uniformly by the same amount and a scale bar is included.

In the absence of cine MRI data, some studies have extracted the reference geometry for FE modeling from tagged MRI[48], eliminating the need to register kinematic and geometric data. However, surface geometries extracted from tagged MRI may overestimate wall thickness due to the difficulty associated with dileneating endocardial borders from trabeculae and papillary muscles. In the absence of local kinematic data, some authors have matched end-daistolic surfaces or volumes[32] to estimate global kinematics, but this method may not adequately constrain the material parameter solution. Subject-specific microstructure, such as that which can be obtained through *in vivo* cDTI is an emerging technique. While cDTI has been validated[49,50], it is not yet widely

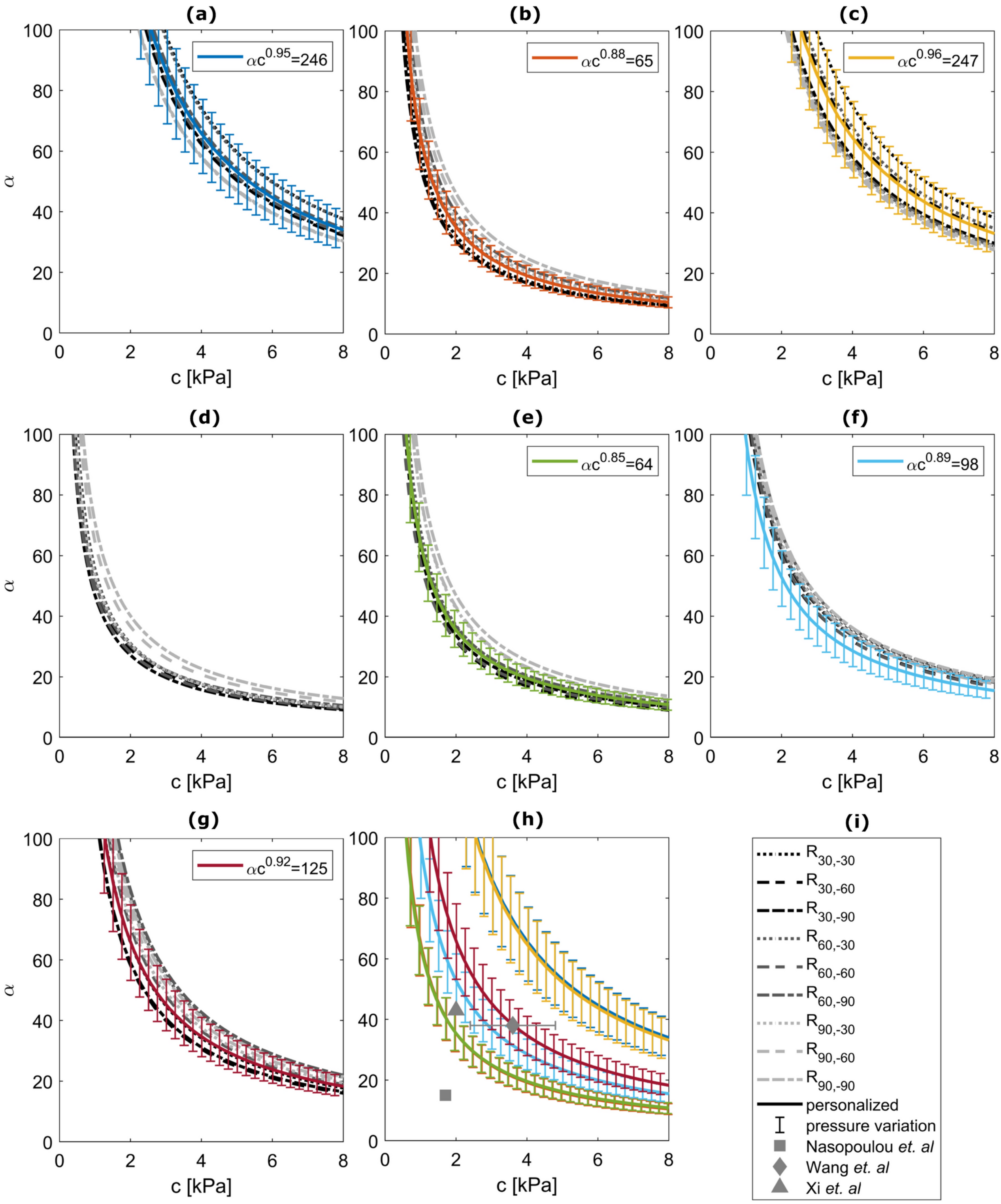

Fig. 8. Optimal c-α coupling curves for each subject (**a**-**g**). A direct comparison of all subjects and a comparison of literature values for passive myocardium parameters in healthy humans appears in (**h**). Solid colored lines are for models with personalized (cDTI) fibers and the uncertain region around this line (colored range bars) represents the upper and lower bounds of the behavior due to a ±20% variation in LV end-diastolic pressure.

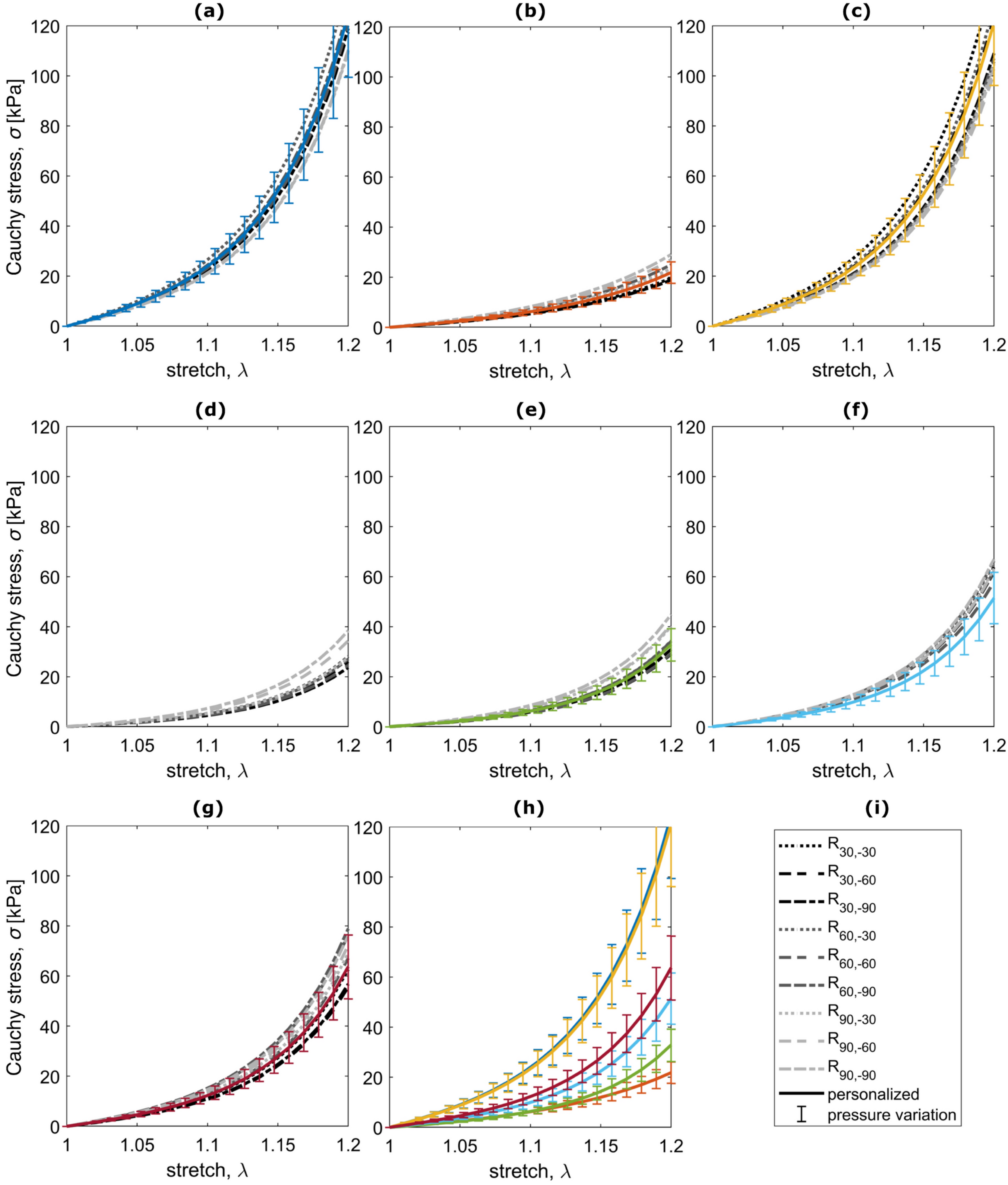

Fig. 9. Comparison of each subject's myocardial stiffness parameter estimation under controlled deformation (**a**-**g**). A direct comparison of all subjects appears in (**h**). Simulations show Cauchy stress vs. stretch from idealized uniaxial tension along the fiber direction for $\alpha = 32$

available in patients or research subjects especially with full LV base-to-apex coverage and with complementary cine MRI and tagged MRI data. Thus, mathematical models of the myofiber orientation are commonly used in the FE models instead[34–36]. While these mathematical fiber descriptions are convenient, there is a lack of studies on the effects of rule-based versus personalized fiber orientations on the final passive myocardial material parameters.

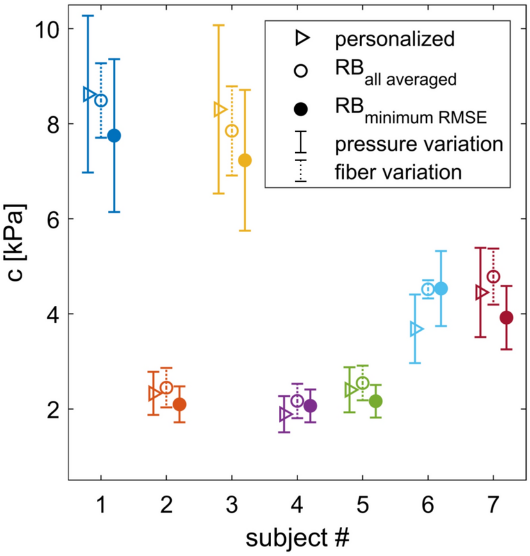

Fig. 10. Comparison of material parameter estimates (c at α=32) between models with personalized cDTI fibers (triangle) vs rule-based fibers (circle). The solid and dotted error bars represent the variation due to end-diastolic pressure (within the expected beat-to-beat range) and rule-based descriptions of fiber orientation, respectively. Generally, the variation in passive myocardial stiffness due to end-diastolic pressure exceeds that which is due to fiber variability

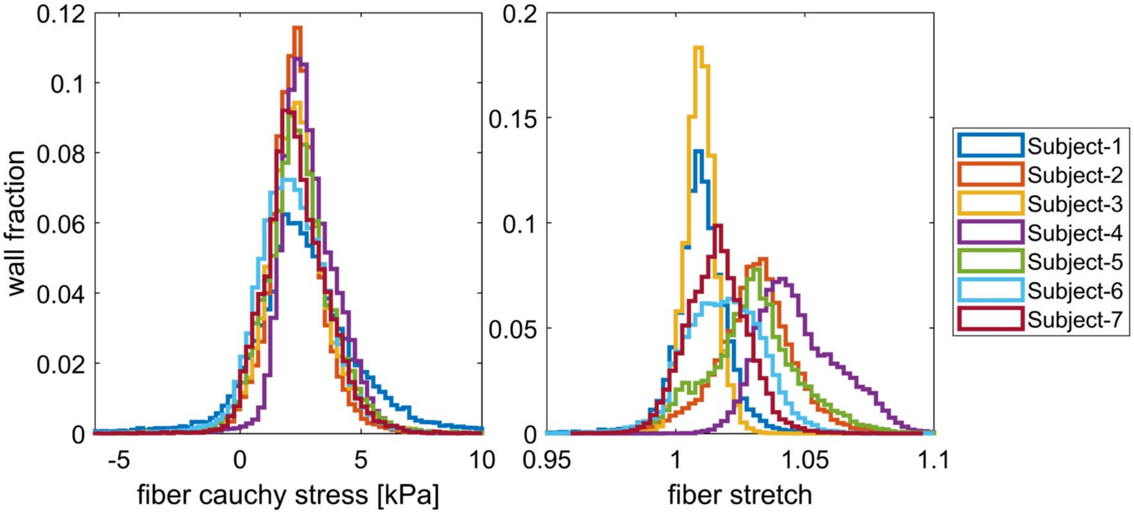

Fig. 11. Fiber Cauchy stress and stretch distribution in the LV myocardium at end-diastole. Wall fraction is the proportion of the myocardial wall experiencing a given fiber stress or stretch relative to the total wall volume

In this study, the parameter estimation is based on a single LV state at end-diastole, which compounds the non-unique solution issue associated with Fung-type exponential constitutive relations such as the Guccione transversely isotropic relation. Despite the availability of multiple tagged MRI imaging frames between diastasis and end-diastole, the absence of LV diastolic pressure measurement precluded the use of kinematic data from multiple cardiac phases for parameter estimation without assuming the form of the diastolic pressure waveform. To better encapsulate the non-uniqueness and correlation of material parameters, for each subject, we obtained an optimal c-α coupling curve for physiological anisotropy ratios. This presentation of the material parameters differs from the more common approach in the literature where only one parameter is calibrated (typically c) while the others are fixed[46]. These optimal c-α coupling curves can be extended to uniquely identify c and α provided corresponding pressure data from at least one additional cardiac phase between diastasis and end-diastole, using the approach introduced by Nasopoulou *et al.*[13].

Results from the Wang and Xi study of healthy *in vivo* passive myocardial material parameters fall within the range of material parameters we obtained, but Nasopoulou's estimates are appreciably softer than the range which we have obtained here (Figs. 8 &12). The discrepancy in material parameters could be reflective of biological

Case	α	***c* (kPa)**			$\lvert\Delta u_{\text{sim}-\text{exp}}\rvert$ **(mm)**			$\lvert\sigma_{\text{fiber}}\rvert$ **(kPa)**			$\lvert\lambda_{\text{fiber}}\rvert$		
		Pers.	RB_{min}	RB_{max}	***Pers.***	RB_{min}	RB_{max}	***Pers.***	RB_{min}	RB_{max}	***Pers.***	RB_{min}	RB_{max}
Subject-1	32	8.7	7.7	9.7	1.92	1.84	1.95	2.64	2.38	2.92	1.010	1.009	1.013
Subject-2	32	2.3	2.0	3.2	1.62	1.53	1.98	2.32	1.86	2.64	1.031	1.017	1.045
Subject-3	32	8.3	7.0	9.7	1.31	1.20	1.37	2.36	2.00	2.66	1.010	1.008	1.013
Subject-4	32		1.8	2.9	2.47	1.97	2.96	2.86	2.18	3.01	1.048	1.022	1.052
Subject-5	32	2.4	2.2	3.1	2.02	1.94	2.38	2.43	2.13	2.76	1.030	1.021	1.043
Subject-6	32	3.7	4.2	4.8	2.49	2.60	2.72	2.18	1.91	2.37	1.019	1.012	1.020
Subject-7	32	4.5	3.9	5.4	1.75	1.71	1.85	2.34	2.16	2.86	1.016	1.012	1.026
Nasopoulou[13]	15	1.7			3.35								
Wang[46]	38	3.6±1.2[a,b]											
Xi[39]	43	2.0[a]			1.78								

Table 3. Passive material parameter estimation results. *c* material parameter at $\alpha = 32$, average displacement error between simulation and experimental nodal positions ($|\Delta u_{\text{sim-exp}}|$), average fiber Cauchy stress ($|\sigma_{\text{fiber}}|$), and average fiber stretch ($|\lambda_{\text{fiber}}|$) for all subjects. Results from models with personalized fibers (*Pers.*) and the minimum (RB_{min}) and maximum (RB_{max}) values across models with rule-based fibers are shown. Results of passive material parameter estimation in healthy humans from the literature included[13,39,46]. [a] Scaling constant defined as half *c* parameter, so values reported here are doubled for consistency. [b] Standard deviation is from 6 subjects.

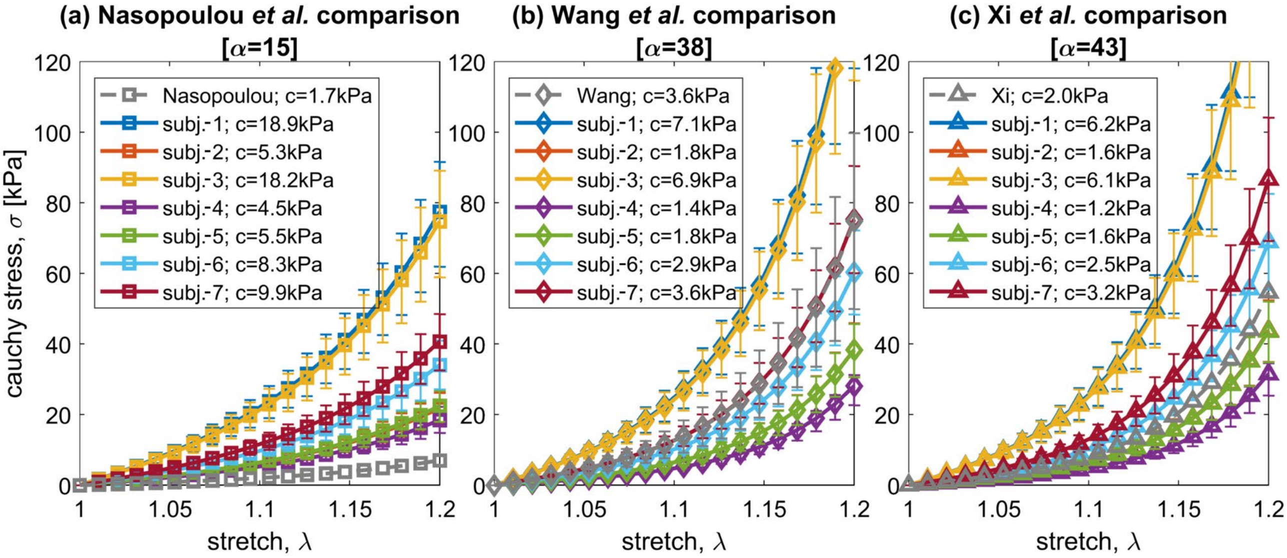

Fig. 12. Comparison of estimated material parameters for all subjects with results from (**a**) Nasopoulou *et al.*[13], (**a**) Wang *et al.*[46] and (c) Xi *et al.*[39] who each performed passive material parameter estimation in healthy humans. Cauchy stress vs. stretch from idealized uniaxial tension along the fiber direction is shown using the corresponding *c* for α from the previous studies

variability in the passive myocardial stiffness of the healthy subjects tested in our respective studies, but it may also be due to different modeling assumptions. Ultimately, extending this myocardial stiffness estimation framework to patients with cardiac conditions characterized by altered passive myocardial stiffness will enable better understanding of the accuracy and precision required to adequately measure important clinical changes to myocardial stiffness properties. For now, the results presented in this study provide an important reference for healthy passive myocardial material parameters that is consistent with prior work.

Turning to the effects of fiber fields and loading pressure, we note that there are relatively few inverse uncertainty quantification analyses assessing the identifiability and variation of inversely estimated material parameters given the uncertainty in the experimental data (e.g., pressures, fiber orientations, kinematics). This task differs from forward uncertainty quantification, where the goal is to establish how uncertainties in the FE model inputs affect the model outputs (quantities of interest). Augenstein *et al.* found that parameter identifiability is affected by the signal-to-noise ratio of the tagged MRI acquisition. Specifically, more image frames are needed for confidence in estimated parameters with increasing noise in the tagged MRI data[51]. Lazarus *et al.* found that some material parameters cannot be reliably identified without inclusion of high pressure data outside of the physiological range[7]. The work of Palit *et al.* is similar to ours, in that they investigated the effects of cardiac geometry, LV end-diastolic pressure, and fiber orientations on material parameter estimation[52]. However, the authors had no kinematic MRI data, and calibrated material parameters using LV volumes, despite the fact that optimizing for material parameters using local deformation kinematics better constrains the parameter estimation. Additionally, the absence of microstructural MRI data meant they couldn't compare between rule-based and personalized fiber orientations. Nevertheless, they found that that the estimated passive material parameters had different degrees of sensitivity to variations in the geometry, pressure, and fiber orientations.

A key finding from our study is that while the use of rule-based descriptions in place of personalized fiber orientations does influence the estimated passive material parameters, the deviation is generally less than that which can be attributed to beat-to-beat variation in the LV end-diastolic pressure. As our results suggest, for the task of identifying passive myocardial material parameters, accurate estimation of the diastolic pressure(s) may be of greater importance than highly accurate microstructural measures. Nevertheless, it is important to note that identification of personalized fiber orientation is still necessary for individuals with heart disease, as structural remodeling may cause significant deviations from rule-based descriptions of fiber orientations[53]. Accurate fiber orientation information is also essential for systolic mechanics[54,55] and for estimating quantities of interest such as myocardial and myofiber stresses and strains[56].

While this study addresses important aspects of estimating passive myocardial stiffness, there are limitations to consider. Firstly, the passive myocardial stiffness estimates obtained in this work were not validated. The patient-specific data used to evaluate *in vivo* passive myocardial stiffness are unavoidably subject to uncertainty that would propagate into the final stiffness estimates. In our previous work, we addressed elements of this validation challenge by implementing a similar MRI and FEM-based passive myocardial stiffness estimation method in isotropic myocardium-mimicking heart phantoms of known stiffness[5]. In that study, we demonstrated that MRI-driven computational constitutive modeling can be used to accurately estimate synthetic heart material stiffnesses in the range of 200-500 kPa. Future work can involve more robust uncertainty quantification and sensitivity analysis for each input used in this study to better understand the precision of our approach.

Additionally, higher performance MRI scanners than those which we used here would enable better quality cDTI images (i.e. higher resolution, higher SNR), enabling more effective evaluation of cardiac microstructure. Although estimated residual stresses in the *in vivo* heart are well documented[57], we did not incorporate this effect and assumed the diastasis cardiac phase corresponding to the start of atrial systole as the unstressed configuration. Algorithms for unloading the prestressed geometry exist[58,59], but they require prior knowledge or assumptions about the material properties as the calculated residual stresses are affected by the chosen material parameters. Additionally, there isn't a universally accepted approach for identifying the residual stresses and current published approaches have yet to be validated using the suite of patient-specific data acquired in our study. Moreover, the lack of an end-diastolic pressure trace meant we did not have the minimum LV pressure, an important piece of information necessary for unloading. Given that the diastasis pressure is generally nonzero and positive, we expect that unloading the models to an unstressed state prior to material parameter calibration would lead to a softening in the estimated passive myocardial stiffness parameters. Furthermore, despite evidence of orthotropy in myocardium, we used a transversely isotropic material model. This is because our cDTI acquisition is mostly sensitive to diffusion in the fiber direction, without providing distinct information about sheetlet orientation. When this data becomes available, the passive stiffness estimation framework could easily be extended to incorporate orthotropic material models. Generally, acquisition of myocardial microstructure with cDTI is challenging, as evidenced by the failure to get adequate personalized fiber orientations in Subject-4. In this subject, we used the $R_{60,-60}$ rule-based description in place of personalized fibers as necessary. Lastly, it is important to acknowledge that currently, both the MRI examination and the subsequent image processing, model building, and material parameter optimization are prohibitively complex and time intensive. Hence, there is a need for efforts focused on streamlining or expediting various aspects of the pipeline.

Conclusion

We developed a method for creating subject-specific *in silico* finite element mechanics models of the LV to evaluate passive myocardial stiffness, by integrating multiphase *in vivo* cardiac cine bSSFP and tagged MRI with single-phase *in vivo* cDTI. The approach was used to characterize the passive myocardial material parameters of seven healthy subjects due to uncertainties in loading pressure and fiber orientation. While variability in fiber orientation influenced the estimation of passive myocardial material parameters, it was overshadowed by the impact of beat-to-beat variability in LV end-diastolic pressures on such estimation.

Data availability

The datasets generated during and/or analysed during the current study are available from the corresponding author on reasonable request.

Code availability

An executable version of the passive material parameter optimization code, along with an example finite element model, is available at the GitHub repository https://github.com/Fikunwa/LV-passive-myocardial-stiffness.

Received: 5 September 2024; Accepted: 4 February 2025

References

1. Zile, M. R., Baicu, C. F. & Gaasch, W. H. Diastolic heart failure-abnormalities in active relaxation and passive stiffness of the left ventricle. *The New England Journal of Medicine* **350**, 1953–1959 (2004).
2. Peirlinck, M. et al. Precision medicine in human heart modeling. *Biomechanics and Modeling in Mechanobiology* **20**, 803–831. https://doi.org/10.1007/s10237-021-01421-z (2021).
3. Wang, V. Y., Nielsen, P. M. F. & Nash, M. P. Image-Based Predictive Modeling of Heart Mechanics. *Annual Review of Biomedical Engineering* **17**, 351–383. https://doi.org/10.1146/annurev-bioeng-071114-040609 (2015).
4. Rodero, C. *et al.* Advancing clinical translation of cardiac biomechanics models: a comprehensive review, applications and future pathways. *Frontiers in Physics* **11**, https://doi.org/10.3389/fphy.2023.1306210 (2023). Publisher: Frontiers.
5. Kolawole, F. O. et al. Validating MRI-Derived Myocardial Stiffness Estimates Using In Vitro Synthetic Heart Models. *Annals of Biomedical Engineering*[SPACE]https://doi.org/10.1007/s10439-023-03164-7 (2023).
6. Rodr-guez-Cantano, R., Sundnes, J. & Rognes, M. E. Uncertainty in cardiac myofiber orientation and stiffnesses dominate the variability of left ventricle deformation response. *International Journal for Numerical Methods in Biomedical Engineering* **35**, e3178 (2019).
7. Lazarus, A., Dalton, D., Husmeier, D. & Gao, H. Sensitivity analysis and inverse uncertainty quantification for the left ventricular passive mechanics. *Biomechanics and Modeling in Mechanobiology* **21**, 953–982 (2022).
8. Peirlinck, M. et al. Kinematic boundary conditions substantially impact in silico ventricular function. *International Journal for Numerical Methods in Biomedical Engineering* **35**, e3151. https://doi.org/10.1002/cnm.3151 (2019).
9. Pfaller, M. R. et al. The importance of the pericardium for cardiac biomechanics: from physiology to computational modeling. *Biomechanics and Modeling in Mechanobiology* **18**, 503–529. https://doi.org/10.1007/s10237-018-1098-4 (2019).
10. Nikou, A. et al. Effects of using the unloaded configuration in predicting the in vivo diastolic properties of the heart. *Computer Methods in Biomechanics and Biomedical Engineering* **19**, 1714–1720 (2016).
11. Marchesseau, S. et al. Preliminary specificity study of the Bestel-Clément-Sorine electromechanical model of the heart using parameter calibration from medical images. *Journal of the Mechanical Behavior of Biomedical Materials* **20**, 259–271 (2013).
12. Nordsletten, D. et al. A viscoelastic model for human myocardium. *Acta Biomaterialia* **135**, 441–457 (2021).
13. Nasopoulou, A. et al. Improved identifiability of myocardial material parameters by an energy-based cost function. *Biomechanics and Modeling in Mechanobiology* **16**, 971–988 (2017).
14. Andersen, O. S. et al. Estimating Left Ventricular Filling Pressure by Echocardiography. *Journal of the American College of Cardiology* **69**, 1937–1948. https://doi.org/10.1016/j.jacc.2017.01.058 (2017).
15. Bieri, O. & Scheffler, K. Fundamentals of balanced steady state free precession MRI. *Journal of Magnetic Resonance Imaging* **38**, 2–11. https://doi.org/10.1002/jmri.24163 (2013).
16. Ennis, D. B. et al. Assessment of regional systolic and diastolic dysfunction in familial hypertrophic cardiomyopathy using MR tagging. *Magnetic Resonance in Medicine* **50**, 638–642. https://doi.org/10.1002/mrm.10543 (2003).
17. Moulin, K. et al. Myofiber strain in healthy humans using DENSE and cDTI. *Magnetic Resonance in Medicine* **86**, 277–292. https://doi.org/10.1002/mrm.28724 (2021).
18. Moulin, K., Verzhbinsky, I. A., Maforo, N. G., Perotti, L. E. & Ennis, D. B. Probing cardiomyocyte mobility with multi-phase cardiac diffusion tensor MRI. *PloS One* **15**, e0241996 (2020).
19. Moulin, K. et al. In vivo free-breathing DTI and IVIM of the whole human heart using a real-time slice-followed SE-EPI navigator-based sequence: A reproducibility study in healthy volunteers. *Magnetic Resonance in Medicine* **76**, 70–82 (2016).
20. Shmuylovich, L., Chung, C. S. & Kovács, S. J. Point: Left ventricular volume during diastasis is the physiological in vivo equilibrium volume and is related to diastolic suction. *Journal of Applied Physiology* **109**, 606–608 (2010).
21. Wang, Z. J. et al. Left Ventricular Diastolic Myocardial Stiffness and End-Diastolic Myofibre Stress in Human Heart Failure Using Personalised Biomechanical Analysis. *Journal of Cardiovascular Translational Research* **11**, 346–356 (2018).
22. Loecher, M., Perotti, L. E. & Ennis, D. B. Using synthetic data generation to train a cardiac motion tag tracking neural network. *Medical Image Analysis* **74**, 102223 (2021).
23. Kellner, E., Dhital, B., Kiselev, V. G. & Reisert, M. Gibbs-ringing artifact removal based on local subvoxel-shifts. *Magnetic Resonance in Medicine* **76**, 1574–1581. https://doi.org/10.1002/mrm.26054 (2016).
24. Smith, S. M. et al. Advances in functional and structural MR image analysis and implementation as FSL. *NeuroImage* **23**(Suppl 1), S208-219 (2004).
25. Coll-Font, J. et al. Manifold-based respiratory phase estimation enables motion and distortion correction of free-breathing cardiac diffusion tensor MRI. *Magnetic Resonance in Medicine* **87**, 474–487. https://doi.org/10.1002/mrm.28972 (2022).
26. Kingsley, P. B. Introduction to diffusion tensor imaging mathematics: Part III. Tensor calculation, noise, simulations, and optimization. *Concepts in Magnetic Resonance Part A* **28A**, 155–179. https://doi.org/10.1002/cmr.a.20050 (2006).
27. Stoeck, C. T., von Deuster, C., Genet, M., Atkinson, D. & Kozerke, S. Second-order motion-compensated spin echo diffusion tensor imaging of the human heart. *Magnetic Resonance in Medicine* **75**, 1669–1676. https://doi.org/10.1002/mrm.25784 (2016).
28. Verzhbinsky, I. A., Magrath, P., Aliotta, E., Ennis, D. B. & Perotti, L. E. Time resolved displacement-based registration of in vivo cDTI cardiomyocyte orientations. In *2018 IEEE 15th International Symposium on Biomedical Imaging (ISBI 2018)*, 474–478, https://doi.org/10.1109/ISBI.2018.8363619 (2018).
29. Perotti, L. E. et al. Estimating cardiomyofiber strain in vivo by solving a computational model. *Medical Image Analysis* **68**, 101932. https://doi.org/10.1016/j.media.2020.101932 (2021).
30. Freytag, B. *et al.* Field-Based Parameterisation of Cardiac Muscle Structure from Diffusion Tensors. In van Assen, H., Bovendeerd, P. & Delhaas, T. (eds.) *Functional Imaging and Modeling of the Heart*, Lecture Notes in Computer Science, 146–154 (Springer International Publishing, Cham, 2015).
31. Bradley, C. et al. OpenCMISS: a multi-physics & multi-scale computational infrastructure for the VPH/Physiome project. *Progress in Biophysics and Molecular Biology* **107**, 32–47 (2011).
32. Stimm, J. *et al.* Personalization of biomechanical simulations of the left ventricle by in-vivo cardiac DTI data: Impact of fiber interpolation methods. *Frontiers in Physiology* **13** (2022).
33. Kolawole, F. O. *et al.* Evaluating Passive Myocardial Stiffness Using in vivo cine, cDTI, and Tagged MRI. In Bernard, O., Clarysse, P., Duchateau, N., Ohayon, J. & Viallon, M. (eds.) *Functional Imaging and Modeling of the Heart*, Lecture Notes in Computer Science, 527–536, https://doi.org/10.1007/978-3-031-35302-4_54 (Springer Nature Switzerland, Cham, 2023).
34. Bayer, J. D., Blake, R. C., Plank, G. & Trayanova, N. A. A novel rule-based algorithm for assigning myocardial fiber orientation to computational heart models. *Annals of Biomedical Engineering* **40**, 2243–2254. https://doi.org/10.1007/s10439-012-0593-5 (2012).
35. Doste, R. et al. A rule-based method to model myocardial fiber orientation in cardiac biventricular geometries with outflow tracts. *International Journal for Numerical Methods in Biomedical Engineering* **35**, e3185. https://doi.org/10.1002/cnm.3185 (2019).
36. Potse, M., Dube, B., Richer, J., Vinet, A. & Gulrajani, R. M. A Comparison of Monodomain and Bidomain Reaction-Diffusion Models for Action Potential Propagation in the Human Heart. *IEEE Transactions on Biomedical Engineering* **53**, 2425–2435. https://doi.org/10.1109/TBME.2006.880875 (2006).
37. Sands, G. B., Smaill, B. H. & LeGrice, I. J. Virtual sectioning of cardiac tissue relative to fiber orientation. *Annual International Conference of the IEEE Engineering in Medicine and Biology Society. IEEE Engineering in Medicine and Biology Society. Annual International Conference* **2008**, 226–229, https://doi.org/10.1109/IEMBS.2008.4649131 (2008).
38. Guccione, J. M., McCulloch, A. D. & Waldman, L. K. Passive material properties of intact ventricular myocardium determined from a cylindrical model. *Journal of Biomechanical Engineering* **113**, 42–55 (1991).

39. Xi, J. et al. The estimation of patient-specific cardiac diastolic functions from clinical measurements. *Medical Image Analysis* **17**, 133–146 (2013).
40. Geuzaine, C. & Remacle, J.-F. Gmsh: A 3-D finite element mesh generator with built-in pre- and post-processing facilities. *International Journal for Numerical Methods in Engineering* **79**, 1309–1331 (2009).
41. Maas, S. A., Ellis, B. J., Ateshian, G. A. & Weiss, J. A. FEBio: finite elements for biomechanics. *Journal of Biomechanical Engineering* **134**, 011005 (2012).
42. Bouchard, R. J., Gault, J. H. & Ross, J. Evaluation of Pulmonary Arterial End-Diastolic Pressure as an Estimate of Left Ventricular End-Diastolic Pressure in Patients with Normal and Abnormal Left Ventricular Performance. *Circulation* **44**, 1072–1079. https://doi.org/10.1161/01.CIR.44.6.1072 (1971).
43. Hasaballa, A. I. *et al.* Automated Estimation of Left Ventricular Diastolic Chamber Stiffness: Application to Patients with Heart Failure and Aortic Regurgitation. In Bernard, O., Clarysse, P., Duchateau, N., Ohayon, J. & Viallon, M. (eds.) *Functional Imaging and Modeling of the Heart*, Lecture Notes in Computer Science, 626–635, https://doi.org/10.1007/978-3-031-35302-4_64 (Springer Nature Switzerland, Cham, 2023).
44. Freytag, B. *et al.* In Vivo Pressure-Volume Loops and Chamber Stiffness Estimation Using Real-Time 3D Echocardiography and Left Ventricular Catheterization - Application to Post-heart Transplant Patients. In Ennis, D. B., Perotti, L. E. & Wang, V. Y. (eds.) *Functional Imaging and Modeling of the Heart*, Lecture Notes in Computer Science, 396–405, https://doi.org/10.1007/978-3-030-78710-3_38 (Springer International Publishing, Cham, 2021).
45. Kawel, N. *et al.* Normal Left Ventricular Myocardial Thickness for Middle-Aged and Older Subjects With Steady-State Free Precession Cardiac Magnetic Resonance. *Circulation: Cardiovascular Imaging* **5**, 500–508, https://doi.org/10.1161/CIRCIMAGING.112.973560 (2012). Publisher: American Heart Association.
46. Wang, V. Y., Young, A. A., Cowan, B. R. & Nash, M. P. Changes in In Vivo Myocardial Tissue Properties Due to Heart Failure. In Ourselin, S., Rueckert, D. & Smith, N. (eds.) *Functional Imaging and Modeling of the Heart*, Lecture Notes in Computer Science, 216–223 (Springer, Berlin, Heidelberg, 2013).
47. Li, Z., Liu, Y., Peña, E., Valdez-Jasso, D. & Tang, D. Editorial: Computational Biomechanics of the Heart and Vasculature With Potential Clinical and Surgical Applications. *Frontiers in Physiology* **13**, https://doi.org/10.3389/fphys.2022.872774 (2022). Publisher: Frontiers.
48. Wang, V. Y. et al. Modelling passive diastolic mechanics with quantitative MRI of cardiac structure and function. *Medical Image Analysis* **13**, 773–784 (2009).
49. Teh, I. et al. Validation of cardiac diffusion tensor imaging sequences: A multicentre test-retest phantom study. *Nmr in Biomedicine* **35**, e4685. https://doi.org/10.1002/nbm.4685 (2022).
50. Aliotta, E., Moulin, K., Magrath, P. & Ennis, D. B. Quantifying precision in cardiac diffusion tensor imaging with second-order motion-compensated convex optimized diffusion encoding. *Magnetic Resonance in Medicine* **80**, 1074–1087. https://doi.org/10.1002/mrm.27107 (2018).
51. Augenstein, K. F., Cowan, B. R., LeGrice, I. J., Nielsen, P. M. F. & Young, A. A. Method and Apparatus for Soft Tissue Material Parameter Estimation Using Tissue Tagged Magnetic Resonance Imaging. *Journal of Biomechanical Engineering* **127**, 148–157. https://doi.org/10.1115/1.1835360 (2005).
52. Palit, A., Bhudia, S. K., Arvanitis, T. N., Turley, G. A. & Williams, M. A. In vivo estimation of passive biomechanical properties of human myocardium. *Medical & Biological Engineering & Computing* **56**, 1615–1631. https://doi.org/10.1007/s11517-017-1768-x (2018).
53. Helm, P. A. *et al.* Evidence of Structural Remodeling in the Dyssynchronous Failing Heart. *Circulation Research* **98**, 125–132, https://doi.org/10.1161/01.RES.0000199396.30688.eb (2006). Publisher: American Heart Association.
54. Barbarotta, L. & Bovendeerd, P. H. M. A Computational Approach on Sensitivity of Left Ventricular Wall Strains to Fiber Orientation. In Ennis, D. B., Perotti, L. E. & Wang, V. Y. (eds.) *Functional Imaging and Modeling of the Heart*, Lecture Notes in Computer Science, 296–304, https://doi.org/10.1007/978-3-030-78710-3_29 (Springer International Publishing, Cham, 2021).
55. Campos, J. O., Sundnes, J., dos Santos, R. W. & Rocha, B. M. Uncertainty quantification and sensitivity analysis of left ventricular function during the full cardiac cycle. *Philosophical Transactions of the Royal Society A: Mathematical, Physical and Engineering Sciences* **378**, 20190381. https://doi.org/10.1098/rsta.2019.0381 (2020).
56. Wang, H. M. et al. Structure-based finite strain modelling of the human left ventricle in diastole. *International Journal for Numerical Methods in Biomedical Engineering* **29**, 83–103. https://doi.org/10.1002/cnm.2497 (2013).
57. Omens, J. H. & Fung, Y. C. Residual strain in rat left ventricle. *Circulation Research* **66**, 37–45 (1990).
58. Wang, Z. J. et al. Efficient estimation of load-free left ventricular geometry and passive myocardial properties using principal component analysis. *International Journal for Numerical Methods in Biomedical Engineering* **36**, e3313. https://doi.org/10.1002/cnm.3313 (2020).
59. Peirlinck, M., De Beule, M., Segers, P. & Rebelo, N. A modular inverse elastostatics approach to resolve the pressure-induced stress state for in vivo imaging based cardiovascular modeling. *Journal of the Mechanical Behavior of Biomedical Materials* **85**, 124–133 (2018).

Acknowledgements

This work was supported by NSF 2205103 and NIH R01 HL131823 to DBE.

Author contributions

FK, VYW, and DBE conceived the study design. DBE developed the imaging approach. VYW, EK, and MPN informed the mechanics approach. FK and TEC conducted the experiments. BF and TEC analyzed the cDTI data. ML analyzed the tagged MRI data. FK and VYW analyzed the results. All authors contributed to the review and finalization of the manuscript.

Declarations

Competing interests

The authors declare no competing interests.

Additional information

Correspondence and requests for materials should be addressed to F.O.K.

Reprints and permissions information is available at www.nature.com/reprints.